


Film levitation and central jet of droplet impact on nanotube surface at superheated conditions

Dongdong Zhou, Yuhui Zhang, Yu Hou, and Xin Zhong*

*State Key Laboratory of Multiphase Flow in Power Engineering, Xi'an Jiaotong University, Shaanxi 710049, China*Jian Jin and Lidong Sun[†]*State Key Laboratory of Mechanical Transmission, School of Materials Science and Engineering, Chongqing University, Chongqing 400044, China* (Received 25 April 2020; revised 5 September 2020; accepted 1 October 2020; published 26 October 2020)

Influences of surface nanotubes at high temperatures are investigated on droplet impact dynamics and Leidenfrost effect. Five distinct regimes of impact droplets are found on the nanotube surface, including contact boiling, film levitation, central jet levitation, central jet, and Leidenfrost phenomenon. The regimes of film levitation, central jet levitation, and central jet are characterized by either film levitation and/or liquid central jet. The regime of Leidenfrost phenomenon is characterized by droplet bounce-off behavior free of any liquid jets. Film levitation is driven by the vaporization of two parts of the droplet, with one as the droplet bottom layer over the contact area above the nanotube structure, and the other as the hemiwicking liquid in nanotubes. Both the vaporization is impaired by increasing the surface temperature, which is attributed to the reduced contact time and less extent of spread of the droplet at a higher surface temperature. The central jet phenomenon is driven by the vapor stream produced by hemiwicking liquid in the central area upon impact. It is enhanced and then suppressed by elevating the surface temperature, resulting from the collective effects of the vapor pressure in nanotubes which increases with the surface temperature, and the cross-sectional area of the vapor stream, which increases and then decreases with the surface temperature. At a high Weber number, the Leidenfrost temperature can be increased by 125°C on the nanotube surface, implying a great potential in heat transfer enhancement for droplet-based applications.

DOI: [10.1103/PhysRevE.102.043108](https://doi.org/10.1103/PhysRevE.102.043108)**I. INTRODUCTION**

Droplet impingement on a high-temperature surface is ubiquitously encountered in diverse applications featuring droplet-based heat transfer processes, including fuel injection [1], steam turbine [2], electronics cooling [3], etc. [4–6]. Once the surface temperature is far beyond the boiling temperature of a liquid droplet, a vapor layer would be produced due to the vaporization of the droplet at its contact region with the hot surface. Such a vapor layer could be so thick to isolate the impact droplet from touching the surface, so the heat transfer to the droplet would be significantly abated. This phenomenon is known as the Leidenfrost effect [7], and the corresponding lowest temperature is Leidenfrost point or Leidenfrost temperature. The emergence of Leidenfrost point normally indicates the commence of heat transfer deterioration, which could result in disfunction and even failure of heat transfer devices. Therefore, great attempts have been devoted to unravel the mechanisms and characteristics of Leidenfrost effect, and to propose strategies to substantially postpone Leidenfrost temperature [8–11].

During a droplet impact onto a high-temperature surface, the Weber number, surface temperature and surface roughness

are three primary factors having significant influences on the dynamics and heat transfer of the droplet [12–15]. Increasing surface temperature enhances vaporization rate of a droplet and leads to various scenarios of the droplet dynamics. For instance, upon increasing the surface temperature, the impact droplet exhibited four distinct regimes, namely film evaporation, nucleate boiling, transition boiling and film boiling [16,17], where film boiling corresponds to the Leidenfrost state. Khavari *et al.* [18] divided the regime of boiling into four phases with increasing the surface temperature, which are spreading, bubbly boiling, fingering boiling, and Leidenfrost point. The wetted area of fingering boiling regime decreased by raising the surface temperature, and ultimately it transitioned to the Leidenfrost regime. As the surface temperature exceeded the Leidenfrost point, the phenomena of film splash and central jet could occur [19,20]. Xu *et al.* [21] found that reducing the surrounding pressure and the molecular weight of the gas can suppress droplet splashing completely, which provides a technique to control the splashing phenomenon [22]. In respect to Weber number, in a number of studies the influence of which mainly manifests in dry impact regimes where liquid-solid contact does not occur [23], exemplified by droplet disintegration [24], rebound [25], and spreading [26], rather than in wet impact regimes where liquid-solid contact occurs [18]. However, some studies show that the Leidenfrost point was delayed by increasing the Weber number [27–29]. The underlying reason is that the vapor layer has to

*zhongxin0521@xjtu.edu.cn

†lidong.sun@cqu.edu.cn

be established within a shorter time, so it requires a higher vaporization rate led by a higher surface temperature.

Surface roughness has been intensively studied for its effect on Leidenfrost effect [30–32]. Micropillars, nanopillars [33], nanofibers [34], and nanotubes [35] have been adopted to elevate the Leidenfrost temperature. The mechanisms mainly include capillarity-driven hemiwicking and enhanced wettability induced by surface roughness [36]. Hemiwicking is a state where a liquid/air interface must develop during liquid infiltrating a porous surface [37]. It is driven by capillary force while resisted by viscous force. Kim *et al.* [38] found that surface micropillars resulted in re-enabled intermittent liquid and solid contacts. The resulting Leidenfrost temperature was increased by 26°C and 51°C than the ones on the plain Au-coated and SiO₂-coated surface, respectively. Moreover, Kwon *et al.* [39] investigated the effect of surface pillar spacing on Leidenfrost temperature, which increased by 100°C as the pillar spacing increased from 20 to 100 μm. They found that a smaller pillar spacing enhanced capillary force for hemiwicking, but meanwhile hindered vapor escape from the gap between the droplet and the hot surface. Leidenfrost temperature thus could be largely determined by the competition between the vapor force and the capillary force in surface structure. Farokhnia *et al.* [40] succeeded in manipulating such a competition by employing a decoupled hierarchical structured surface, and on which the Leidenfrost temperature was much higher than those on other hierarchical structured surfaces. A recent study of Tong *et al.* [41] showed a unique lift-off phenomenon of a liquid film on a nanotube surface, which was given rise by the improved wettability and capillary effect of the nanotube structure. Hu *et al.* [42] reported a superhydrophilic surface by fabricating aluminum oxide (AAO) nanoporous, and they showed that the vapor film on this surface was highly thinner and exhibited less dynamic fluctuations. Due to the enhanced surface wettability, the Leidenfrost point for nanoporous surface increased by 32°C. In addition, on a nanofiber surface, Nair *et al.* [43] pointed out that the time scale for the cooling of a nanofiber is smaller than the one for the heat flow inside the nanofiber, so the nanofiber was cooled by the vapor flow prior to the impact of the droplet, and the Leidenfrost temperature was increased.

The aforementioned studies indicate that surface micro- or nanostructures affect droplet dynamics and Leidenfrost point from multiple aspects, such as the enhanced wettability, capillary actions, and cooling of surface structures by vapor flow. In this study, we show that the vaporization of the impact droplet gives rise to the unique phenomena of film levitation and central jet on the nanotube surface. Dependencies of the vaporization for film levitation and central jet on surface temperature are distinctly different, which lead to five regimes of the droplet with an increase of the surface temperature. The mechanism for the transition from the central jet of droplet to Leidenfrost point is also revealed. The Leidenfrost temperature can be postponed by 50°C on such a nanotube surface at a low Weber number, while over 125°C at high Weber numbers. This study reveals the nanotube-induced unique interaction between vaporization and droplet behaviors, which could enrich the knowledge of droplet impact thermodynamics, and has a potential to be employed for techniques demanding heat transfer enhancement.

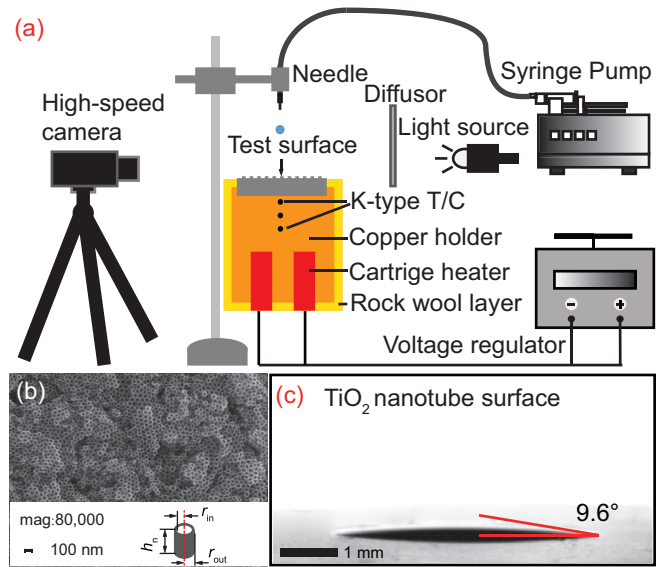


FIG. 1. (a) Schematics of the experimental setup, (b) scanning electron microscope (SEM) image of the TiO₂ nanotubes and the geometric parameters of a nanotube with its interior radius r_{in} , exterior radius r_{out} , and average height h_n , and (c) the static contact angle of 9.6° of the 1 μl water droplet on the nanotube surface at the room temperature.

II. EXPERIMENTAL METHODS

The experimental setup for the droplet impact onto the high-temperature surface is shown in Fig. 1(a). The liquid employed was pure ethanol with its density ρ_l of 789.34 kg/m³, surface tension σ of 22.41×10^{-3} N/m and dynamic viscosity μ_l of 1.19×10^{-3} N s/m² at the atmospheric pressure P_a of 1.01×10^5 Pa and room temperature T_0 of $21 \pm 1^\circ\text{C}$. The ethanol liquid was slowly pushed out of the needle tip by the syringe pump (Harvard, PHD-UTtra). Droplet was formed and detached from the needle tip as the gravity exceeded surface tension, and the droplet initial diameter D_0 was 1.62 ± 0.02 mm. The time the droplet impacted on the hot surface was set as $t = 0$ ms, and the impact velocity v_0 at the same moment was varied by changing the needle distance to the surface. The corresponding Weber number ($We = \rho_l v_0^2 D_0 / \sigma$) changed from 16 to 144. The velocity v_0 was measured from the images captured by using a high-speed camera (FASTCAM Mini AX100) at the speed of 21 600 fps with a 60 mm f/2.8D Nikon lens [41]. $v_0 = \frac{X_{3f}}{t_{3f}}$, where, X_{3f} is the moving distance of the droplet within 3 frames right before impact and t_{3f} is the elapsed time of 3 frames. The droplet impact process was recorded from a side view by the high-speed camera.

Two surfaces were employed. One was a titanium substrate grew with titanium oxide (TiO₂) nanotubes (NTS), and the other was a plain titanium surface (PTS) as the control group. The TiO₂ nanotube surface was obtained by anodic oxidation of a plain titanium surface [44], and its scanning electron microscope (SEM) image is shown in Fig. 1(b). The average interior radius r_{in} , the average exterior radius r_{out} and the average height h_n with deviations of the nanotubes is 24 ± 3.5 nm, 31.5 ± 3.5 nm, and 1.62 ± 0.12 μm, respectively. The static

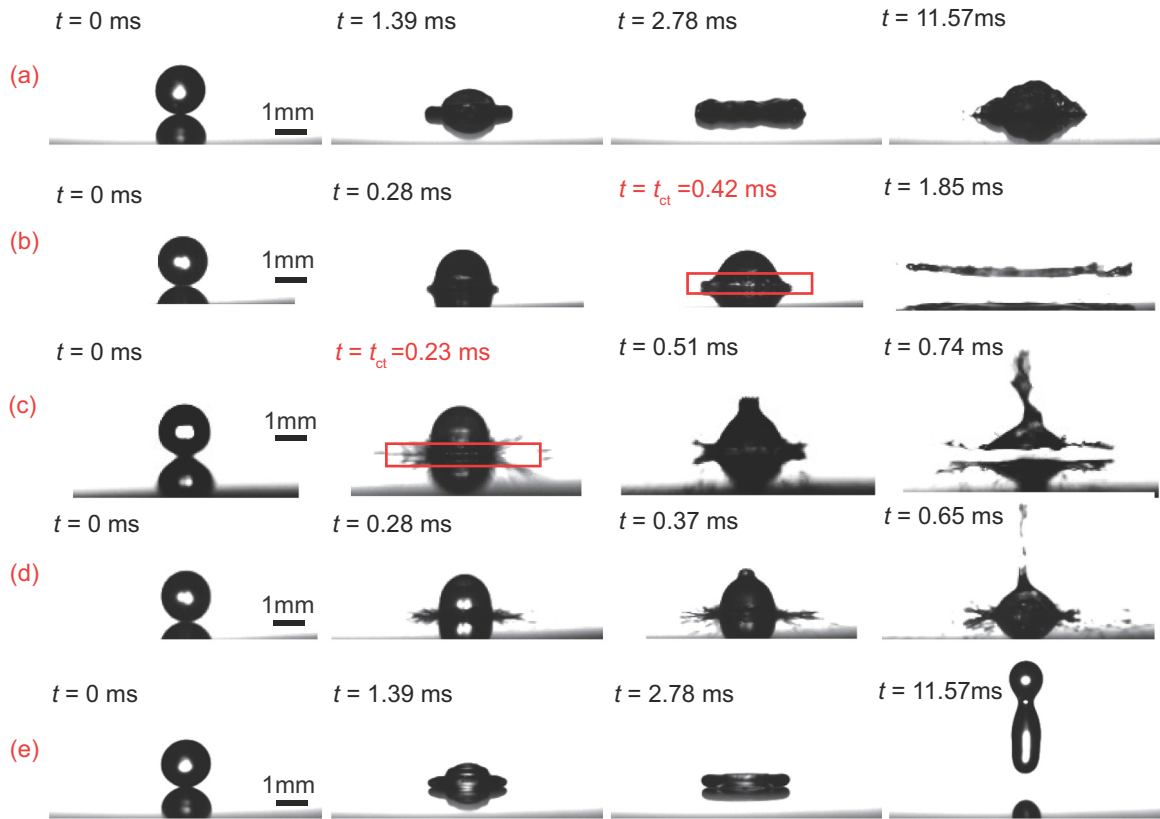


FIG. 2. Time-lapse images of an ethanol droplet impacting onto a nanotube surface (NTS) under different We and surface temperatures T_w . (a) $We = 62$, $T_w = 160^\circ\text{C}$, (b) $We = 62$, $T_w = 170^\circ\text{C}$, (c) $We = 45$, $T_w = 210^\circ\text{C}$, (d) $We = 62$, $T_w = 250^\circ\text{C}$, and (e) $We = 17$, $T_w = 280^\circ\text{C}$. The red frames in (b) and (c) indicate the beginning of vaporization-induced levitation of the droplet. See Supplemental Material Fig. S1 for the five droplet regimes at different T_w and We [45].

contact angle θ of a $1\ \mu\text{L}$ ethanol droplet on NTS was approximately 0° , indicating complete wetting. To reflect the wettability of the NTS, we also measured the static contact angle of a $1\ \mu\text{L}$ deionized water droplet, which is about 9.6° as shown in Fig. 1(c). To guarantee that the surface was not polluted by impurities in the air, the TiO_2 nanotube surface was treated by plasma cleaning for 20 min right before each test, and we measured that θ was almost 0° for an ethanol droplet as well after the experiment was finished. Three k-type thermocouples (Omega, accuracy: $\pm 0.1\ \text{K}$) were inserted along the axis of the copper holder, and were 0.5 mm, 1.5 mm, and 2.5 mm, respectively, below the copper holder top surface. Surface temperature T_w obtained based on the three measurements varied from 100°C to 300°C for both surfaces. To minimize heat leakage, the copper holder was insulated with 20-mm-thick rock wool.

III. RESULTS AND DISCUSSION

A. Dynamics of impact droplets

The droplet shows five impact regimes on NTS with varying T_w and We . Fig. 2(a) shows the contact boiling regime (CB) with T_w at 160°C and We at 62. After the impact, intense boiling occurs at 11.57 ms, where a large number of bubbles are generated. As T_w increases to be above 170°C , the droplet exhibits the film levitation regime (FL), as shown in Fig. 2(b). The droplet spreads at first and then bounces off the surface at

0.42 ms. We define the moment when the droplet first bounces off the surface as the contact time t_{ct} . As it reaches 1.85 ms, the droplet is shaped like a levitating film parallel to the substrate. Moreover, some weak jets occur around the contact area of the droplet, which become intensified at a higher T_w . As T_w further increases to 200°C and higher, the droplet impact regime transits to central jet levitation (CJL). The greatly enhanced liquid jets around the periphery of the contact area are brought in advance, and they occur slightly ahead of the commence of levitation for both FL and CJL regimes. Moreover, a liquid jet is emerged at the droplet center at around 0.51 ms. The droplet as a whole begins to levitate from the substrate at around 0.23 ms when a fairly thin space emerges between the droplet and the substrate, and the levitation phenomenon becomes distinct at 0.74 ms [see Fig. 2(c)]. It is worth noticing that the contact time decreases from 0.42 ms at $T_w = 170^\circ\text{C}$ to 0.23 ms at $T_w = 210^\circ\text{C}$, suggesting that the liftoff phenomenon is brought in advances at a higher T_w . When T_w increases to reach and be higher than 240°C , the impact regime is changed to central jet (CJ). As shown in Fig. 2(d), at 0.65 ms the droplet center is pierced with a formation of a fractured liquid jet. Less drastic liquid jets also emerge around the contact area rim. As T_w is high (280°C) and We is low ($We = 17$), the droplet exhibits Leidenfrost phenomenon (LP) regime. As shown in Fig. 2(e), the droplet spreads to a film, recoiling and bounces off the surface. Different from the former four regimes, neither intensive boiling nor jets were

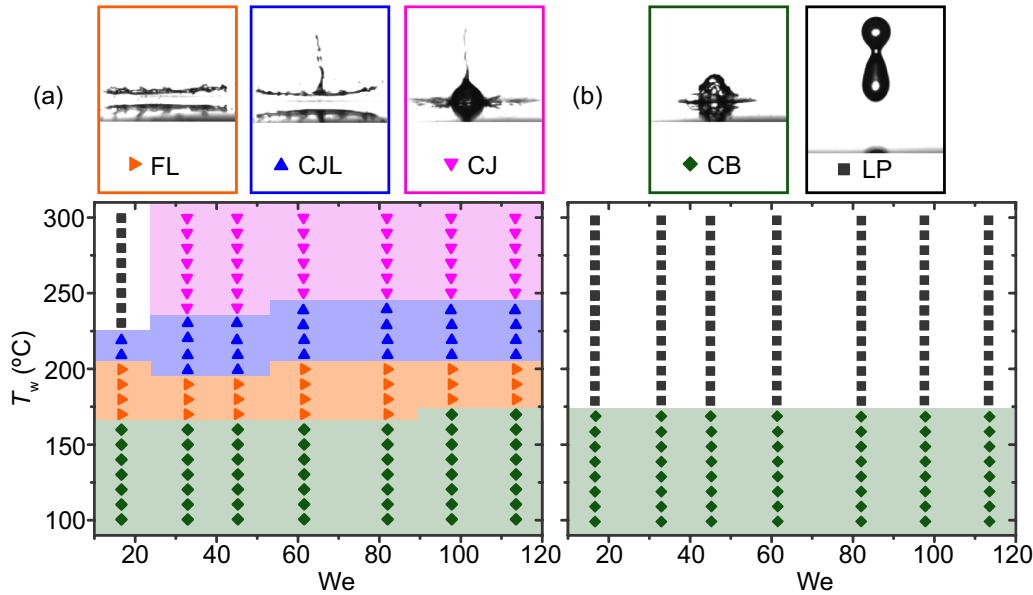


FIG. 3. Phase diagram of the droplet regimes on (a) a nanotube surface (NTS) and (b) a plain titanium surface (PTS) under various surface temperature T_w and the Weber number.

observed throughout. LP regime is a resemblance to the case of a water droplet impacting onto a superhydrophobic surface under a low We [46]. We conjecture that the Leidenfrost point was reached, so there should have a thin vapor layer formed separating the droplet and the surface to enable the trampoliner behavior.

B. Conditions for emergence of droplet regimes

On NTS, the five droplet regimes occurred under different We and T_w . To reflect the influence of the nanotube structure, we conducted similar tests on PTS under the same We and T_w ranges. The ranges of We and T_w for the occurrence of the regimes on NTS and PTS are, respectively, shown in Figs. 3(a) and 3(b). Different from NTS, only CB and LP regimes emerge on PTS. Therefore, FL, CJL, and CJ regimes not appearing on PTS are inferred attributed to nanotubes. As shown in Figs. 3(a) and 3(b), the Leidenfrost point which occurs at 180°C on PTS is postponed to 230°C on NTS with the same $We = 17$.

On PTS, the transit from CB to LP regime occurs at $T_w = 170^\circ\text{C}$, and the transit is insensitive to We . On NTS, with an increase of T_w , the regime transits in such a sequence of CB, FL, CJL and LP for the low $We = 17$. The transition sequence becomes CB, FL, CJL, and CJ at the high $We = 33$. It is expected that by keeping increasing T_w , the regime CJ would eventually transit to LP. This phenomenon did not occur in this study since the upper limit of T_w was restrained to 300°C to prevent nanotubes from melting, and below which the Leidenfrost phenomenon was not initiated. It can be seen that with $We = 17$, the Leidenfrost temperature is enlarged by 50°C, and it is increased by at least 125°C with We higher than 33. Later in this article we interpret the mechanism for the postponed Leidenfrost point by raising We .

C. Mechanisms of film levitation

Film levitation solely emerging on NTS rather than PTS is induced by NTS surface characteristics. NTS is more hydrophilic as compared to PTS in this study, so droplet spread can be enhanced and the resulting heat transfer area between the droplet and the surface is larger. Figure 4(a) shows the contact diameter of droplet D_t as a function of time t for both NTS and PTS with $T_w = 170$ and 180°C , and $We = 62$. D_t is the captured macroscopic contact diameter of the droplet with the substrate by the high-speed camera, which does not reflect the nanostructure, as illustrated in Fig. 4(a). The maximum D_t is the maximum value of D_t , which is namely the contact diameter right before the droplet bounces off the surface. Under the same T_w , D_t is remarkably higher, and its increasing rate is larger on NTS. The greatly enhanced spreading on NTS indicates a larger heat transfer area between the droplet and the surface, so vaporization over the contact area can be intensified which contributes to film levitation. Moreover, as the droplet is spreading on NTS, liquid could fill the nanotubes through hemiwicking. Once the immersed liquid is vaporized, the produced vapor could be a source of the driving force for film levitation as well.

Interestingly, film levitation is negatively dependent on T_w . Figure 4(b) shows the maximum central height of the droplet bottom h_{bmax} as a function of T_w under various We on NTS. h_{bmax} reflects the degree of film levitation, and it decreases with increasing T_w for a specific We . It suggests that the vaporization-induced driving force for film levitation is abated upon raising T_w . In addition, h_{bmax} is basically higher at a larger We . Under a specific T_w , a larger We indicates a higher inertia of the droplet, which results in enhanced spreading and the associated contact area for vaporization, and thus the film levitation could be intensified.

Based on the experimental results, it is conjectured that the vaporization of droplet on NTS driving film levitation is

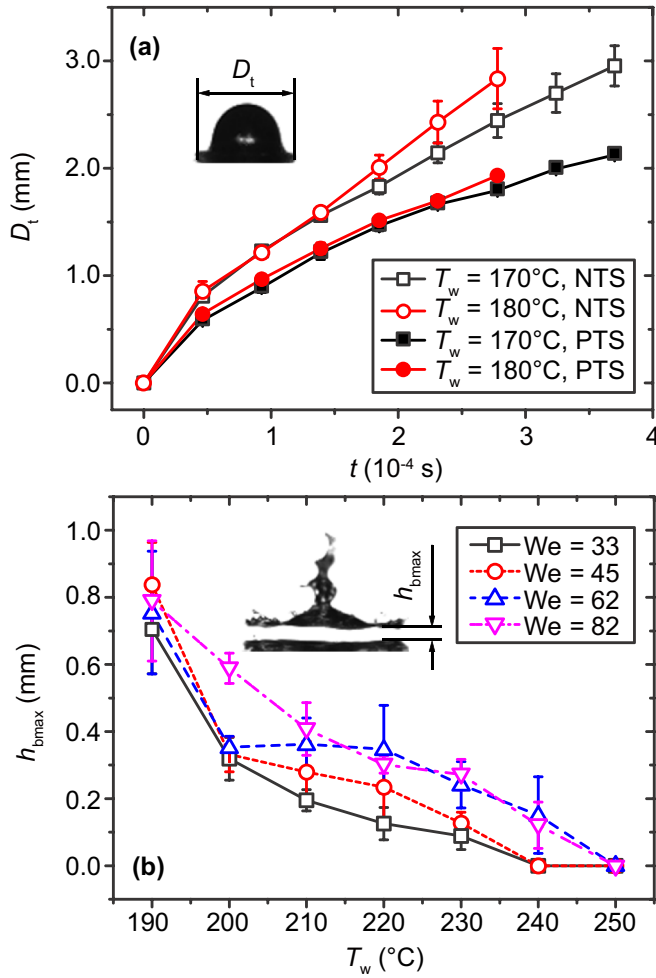


FIG. 4. (a) Contact diameter, D_t , as a function of time t for the nanotube surface (NTS) and the plain titanium surface (PTS) under $T_w = 170^\circ\text{C}$ and 180°C at $We = 62$. (b) Effect of the surface temperature T_w on the maximum height of the droplet bottom $h_{b\max}$ at different We .

comprised of two parts. One is the vaporization of droplet bottom layer over the contact area above the nanotube structure. This part should also be responsible for droplet detachment on PTS. The other part is the vaporization of liquid hemiwicking in nanotubes along with impact and spread. The vapor stream produced from massive nanotubes could bear a high kinetic energy to push droplet away from the surface. Moreover, vaporization of hemiwicking liquid at the central contact area could give rise to the central jet, as observed in the regimes of CJL and CJ at high T_w , and which is elaborated later in this article. The two parts of vaporization are both T_w dependent, and they collectively determine the unique behavior of film levitation of the impact droplet.

1. Vaporization of droplet above nanotube structure

During the contact time and over the contact area, the heat conduction through the nanotube layer is mainly dissipated by heat convection and conduction in the droplet, and the latent heat for vaporization of the droplet bottom layer. The schematic diagram of the heat transfer mode is shown in

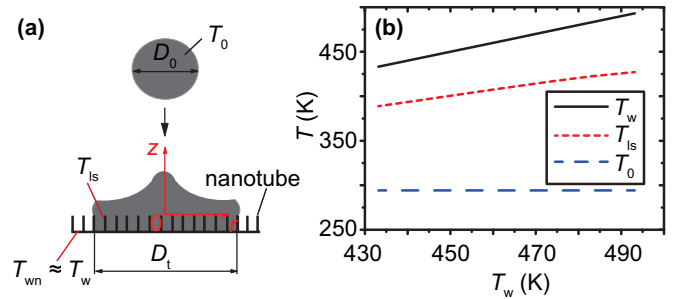


FIG. 5. (a) Schematic diagram of the heat transfer mode for an impact droplet with the droplet initial temperature T_0 , initial diameter D_0 , the solid-liquid interface temperature T_{ls} , the solid surface temperature T_w , and the temperature of nanotubes T_{wn} ($T_{wn} \approx T_w$). (b) The relation among T_{ls} , T_w , and T_0 .

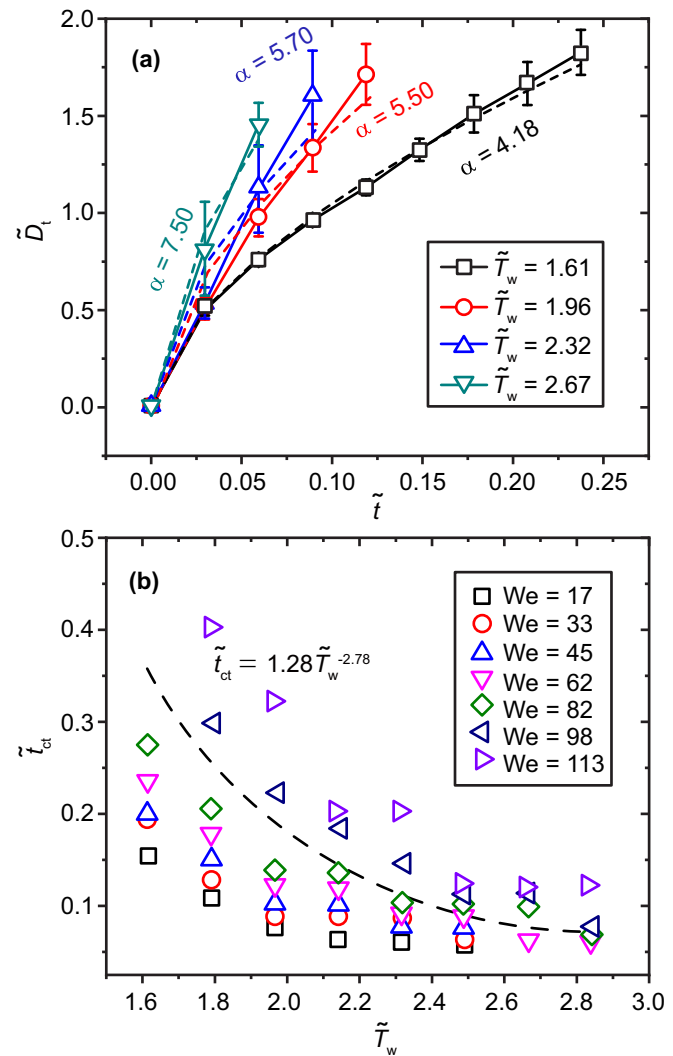


FIG. 6. (a) The normalized contact diameter \tilde{D}_t as a function of the normalized time \tilde{t} at $We = 62$ for various normalized surface temperature \tilde{T}_w ; (b) the normalized contact time \tilde{t}_{ct} as a function of the normalized surface temperature \tilde{T}_w for various We on the nanotube surface (NTS).

Fig. 5(a). By neglecting heat conduction in the droplet for simplicity, the heat transfer through the contact area is (the unit of temperatures is K in the following calculation)

$$\int_0^{t_{\text{ct}}} \frac{[A_t(T_{\text{wn}} - T_{\text{ls}})k_{\text{ln}}^*]}{h_n} dt \approx \int_0^{t_{\text{ct}}} A_t \psi (T_{\text{ls}} - T_0) dt + m_b L, \quad (1)$$

where $A_t = \frac{\pi D_t^2}{4}$ is the macroscopic planar contact area between the droplet and the substrate which does not involve surface porosity (the hemiwicking process is elucidated later in this article). T_{wn} is the temperature of nanotubes by assuming that $T_{\text{wn}} \approx T_w$, T_{ls} the solid-liquid interface temperature, k_{ln}^* the effective thermal conductivity of the liquid and nanotube, ψ the heat transfer coefficient of convection, T_0 the droplet temperature before impact, m_b the mass of liquid which is vaporized, and L is the latent heat of vaporization. The expression of k_{ln}^* [47] is

$$k_{\text{ln}}^* = \left(\frac{r_{\text{in}}}{r_{\text{out}}}\right)^2 k_l + \left[1 - \left(\frac{r_{\text{in}}}{r_{\text{out}}}\right)^2\right] k_n, \quad (2)$$

where k_l and k_n are the thermal conductivity of the liquid and nanotube, respectively. According to Ref. [48], the relation between T_{ls} and T_w can be estimated by

$$T_{\text{ls}} = aT_w + T_0 b, \quad (3)$$

where $a = \frac{\sqrt{k_n \rho_n c_{p,n}}}{\sqrt{k_n \rho_n c_{p,n}} + \sqrt{k_l \rho_l c_{p,l}}}$ and $b = \frac{\sqrt{k_l \rho_l c_{p,l}}}{\sqrt{k_n \rho_n c_{p,n}} + \sqrt{k_l \rho_l c_{p,l}}}$. ρ_n and $c_{p,n}$ are the density and specific heat capacity of nanotube material, respectively. $c_{p,l}$ is the specific heat capacity of the

liquid at the atmospheric pressure. We plot in Fig. 5(b) the relation among T_{ls} , T_w and T_0 . T_{ls} is much closer to T_w because of the large magnitude of $k_n \rho_n c_{p,n}$, and it increases with T_w .

From the experimental results, we obtained the relation of the normalized contact diameter $\tilde{D}_t = \frac{D_t}{D_0}$ with the normalized time $\tilde{t} = \frac{v_0}{D_0} t$, and the one of the normalized contact time $\tilde{t}_{\text{ct}} = \frac{v_0}{D_0} t_{\text{ct}}$ with the normalized surface temperature $\tilde{T}_w = \frac{T_w - T_{v,a}}{T_{v,a} - T_0}$ for the cases with $We = 62$ as an example, where $T_{v,a}$ is the saturation temperature of ethanol at the atmospheric pressure. As shown in Fig. 6(a), the relation of \tilde{D}_t and \tilde{t} under a \tilde{T}_w is fitted by the equation $\tilde{D}_t \approx \alpha \tilde{t}^{0.6}$, $\alpha \approx 2.87 \tilde{T}_w - 0.41$. Therefore, the normalized contact area \tilde{A}_t is

$$\tilde{A}_t = \frac{A_t}{A_0} \approx (2.06 \tilde{T}_w^2 - 0.59 \tilde{T}_w + 0.04) \tilde{t}^{1.2}, \quad (4)$$

where $A_0 = \pi D_0^2$. \tilde{T}_w affects the fitting equation of \tilde{D}_t with \tilde{t} , such that a higher \tilde{T}_w leads to a larger α .

In Fig. 6(b), we plot the normalized contact time \tilde{t}_{ct} versus \tilde{T}_w for NTS with different We . The fitting equation of \tilde{t}_{ct} as a function \tilde{T}_w is

$$\tilde{t}_{\text{ct}} = 1.28 \tilde{T}_w^{-2.78}. \quad (5)$$

It can be seen that \tilde{t}_{ct} is negatively dependent on \tilde{T}_w , and the order of magnitude of corresponding t_{ct} is 10^{-4} s.

Substituting Eqs. (3), (4), and (5) to Eq. (1), we have

$$\tilde{m}_b = B_1 \tilde{T}_w^{-3.12} + B_2 \tilde{T}_w^{-4.12} + B_3 \tilde{T}_w^{-5.12} + B_4 \tilde{T}_w^{-6.12}, \quad (6)$$

where $\tilde{m}_b = \frac{m_b}{m_0}$ is the normalized vaporization mass of the liquid, in which $m_0 = \frac{1}{6} \pi D_0^3 \rho_l$ is the initial mass of the droplet,

$$\begin{aligned} B_1 &= \frac{7.21 \times 10^{-11} (k_{\text{ln}}^* c_{p,l} T_0 - k_{\text{ln}}^* c_{p,l} T_0 a - \psi h_n c_{p,l} T_0 a)}{L k_{l,a}}, \\ B_2 &= \frac{4.23 \times 10^{-10} (k_{\text{ln}}^* c_{p,l} T_0 - k_{\text{ln}}^* c_{p,l} T_0 a - \psi h_n c_{p,l} T_0 a) - 3.72 \times 10^{-10} (k_{\text{ln}}^* c_{p,l} T_0 b + \psi h_n c_{p,l} T_0 b - \psi h_n c_{p,l} T_0)}{L k_{l,a}}, \\ B_3 &= \frac{1.06 \times 10^{-10} (k_{\text{ln}}^* c_{p,l} T_0 b + \psi h_n c_{p,l} T_0 b - \psi h_n c_{p,l} T_0) - 1.25 \times 10^{-10} (k_{\text{ln}}^* c_{p,l} T_0 - k_{\text{ln}}^* c_{p,l} T_0 a - \psi h_n c_{p,l} T_0 a)}{L k_{l,a}}, \\ B_4 &= \frac{9.17 \times 10^{-12} (k_{\text{ln}}^* c_{p,l} T_0 - k_{\text{ln}}^* c_{p,l} T_0 a - \psi h_n c_{p,l} T_0 a) - 7.68 \times 10^{-12} (k_{\text{ln}}^* c_{p,l} T_0 b + \psi h_n c_{p,l} T_0 b - \psi h_n c_{p,l} T_0)}{L k_{l,a}}, \text{ and} \end{aligned}$$

$k_{l,a}$ is the thermal conductivity of the liquid at room temperature and atmospheric pressure.

Equation (6) indicates that the vaporization of droplet bottom above the nanotube structure is inversely dependent on \tilde{T}_w , which partially explains the attenuated levitation behavior at a high \tilde{T}_w .

2. Vaporization of hemiwicking liquid in nanotubes

During the spread of an impact droplet on NTS, liquid could fill nanotubes through hemiwicking. The liquid in nanotubes, once vaporized, could contribute to drive film levitation, as well as a liquid central jet. Herein we examine the process of vaporization of liquid hemiwicking in nanotubes and its dependence on T_w by comparing the time scales of spreading t_{spr} , hemiwicking in a nanotube t_{hw} , and complete vaporization of liquid filling a nanotube t_{ev} .

Amid spread, the time for the film front to reach a nanotube at a distance $r = \frac{D_t}{2}$ from the origin of impact is denoted as t_{spr} , and t_{spr} is t before the droplet lift-off. Once the liquid front reaches the nanotube, hemiwicking could occur. In the

process of hemiwicking, the liquid is acted by capillary force, viscous force and inertial force. First, a scaling law is used to analyze the flow in a single nanotube for $We = 62$. The capillary force is scaled as $2\pi r_{\text{in}} \sigma$. The viscous force is scaled as $\mu_1 h_1 \frac{\partial h_1}{\partial t}$, where h_1 is the imbibition height from the nanotube top surface, and we consider the case of full hemiwicking, so $h_1 = h_n$. $\frac{\partial h_1}{\partial t} = v_1$, where v_1 is the velocity of the liquid, and we assume that v_1 approximately equals to v_0 ($v_1 \approx v_0$). The ratio of the capillary force to the viscous force is about $\frac{2\pi r_{\text{in}} \sigma}{\mu_1 h_n v_0} \sim 10^0$, namely, the capillary force is at the same order of the viscous force. The inertial force is scaled as $V_n \rho_l v_1 \frac{\partial v_1}{\partial z}$, where V_n is the interior volume of a nanotube and $\frac{\partial v_1}{\partial z} \approx \frac{v_0}{h_n}$. The ratio of the capillary force to the inertial force is about $\frac{2\sigma}{r_{\text{in}} \rho_l v_0^2} \sim 10^2$. It can be seen that the capillary force and the viscous force are two orders of magnitude times higher than the inertial force, so the inertial force can be neglected. The rate of hemiwicking is thus mainly determined by the balance between capillary force as the driving force, and the viscous force as the

resistance. This force balance gives $t \sim (h_1^2 \mu_1)/(4\pi r_{in} \sigma)$ [49], and by replacing h_1 with the height of a nanotube h_n we obtain the time scale of full hemiwicking $t_{hw} \sim (h_n^2 \mu_1)/(4\pi r_{in} \sigma)$. Figure 4(a) shows that t_{spr} is at the order of 10^{-4} s at $We = 62$. t_{hw} is scaled as 10^{-7} s, and it is orders of magnitude smaller than t_{spr} , suggesting that the full hemiwicking of a nanotube is completed instantaneously right after the arrival of the film front.

The time scale of vaporization of liquid filling a nanotube, t_{ev} , can be evaluated by the relation that the latent heat of vaporization is mainly from the heat conduction through the nanotube wall, so the vaporization rate \dot{m} is expressed as

$$\dot{m} = \frac{k_{vn}^* \Delta T \pi r_{in}^2}{L^* h_v}, \quad (7)$$

in which k_{vn}^* is the effective thermal conductivity of the vapor and nanotube, $\Delta T = T_w - T_0$, L^* the effective latent heat of vaporization, and h_v is the instantaneous height of vapor in a nanotube. The expression of k_{vn}^* [47] and L^* [50] are, respectively,

$$k_{vn}^* = \left(\frac{r_{in}}{r_{out}}\right)^2 k_v + \left[1 - \left(\frac{r_{in}}{r_{out}}\right)^2\right] k_n \quad (8)$$

and

$$L^* = L + c_{p,l} \frac{T_w - T_{v,a}}{2}, \quad (9)$$

where k_v is the thermal conductivity of vapor.

According to Eq. (6), \dot{m} is inversely proportional to the vapor thickness h_v . The mass of liquid immersed in a nanotube is $m_n = \rho_{l,a} \pi r_{in}^2 h_n$, where $\rho_{l,a}$ is the liquid density at P_a and the room temperature. At $h_v = h_n/2$ for instance, the corresponding vaporization rate $\dot{m} = (2k_{vn}^* \Delta T \pi r_{in}^2)/(L^* h_n)$, and t_{ev} at this rate is

$$t_{ev} = \frac{m_n}{\dot{m}} = \frac{\rho_{l,a} h_n^2 L^*}{2k_{vn}^* \Delta T}. \quad (10)$$

With T_w increasing from 170°C to 240°C , the order of magnitude of t_{ev} decreases from 10^{-6} s to 10^{-7} s. Herein the cases for T_w higher than 240°C are not analyzed since the corresponding physical properties of ethanol are unattainable. But still it is rational to presume that t_{ev} would decrease further as T_w keeps increasing.

t_{hw} is an order of magnitude smaller than t_{ev} at a low T_w , while they are at the same order of magnitude at a high T_w . It demonstrates that at a lower T_w , hemiwicking could be largely finished ahead of vaporization, while at higher T_w , vaporization could occur simultaneously with hemiwicking. The reduced t_{ev} at a higher T_w is evidenced by the experimental observation of peripheral jets of droplet contact area exclusively on NTS. As shown in the inset of Fig. 7, small jets around the periphery of the contact area along with spreading are observed on NTS, which are caused by the vapor escape produced by hemiwicking liquid. Figure 7 shows that the time when the jets first appear t_{pj} is in the order of $10^{-5} \sim 10^{-4}$ s, which is approximately two orders of magnitude higher than t_{ev} . The commence of peripheral jets could reflect the flow of a massive vaporization of liquid immersed in nanotubes. Most importantly, t_{pj} decreases upon increasing T_w , namely, peripheral jets emerge earlier at a higher T_w . A higher T_w

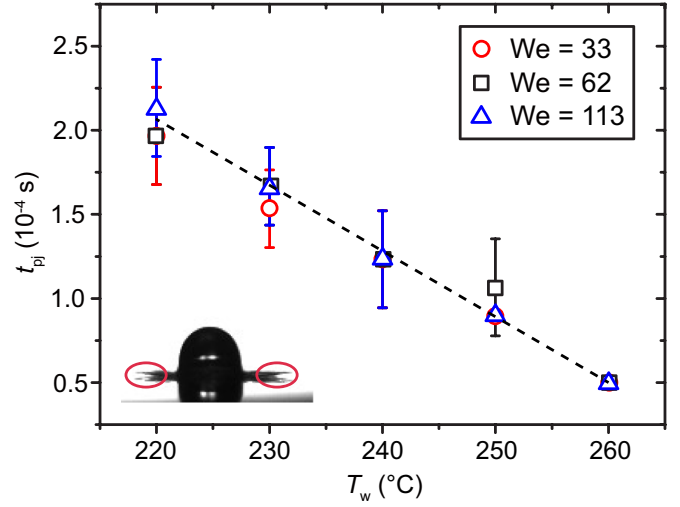


FIG. 7. The time at the beginning of peripheral jets, t_{pj} , as a function of T_w at We of 33, 62, and 113. The inset images shows the droplet with peripheral jets.

indicates a higher \dot{m} and a shorter t_{ev} , so peripheral jets are brought in advance.

It is found that the relative rate of droplet spreading and vaporization of hemiwicking liquid is critical to droplet levitation as well as central jet. Figure 8(a) demonstrates $r = \frac{D_t}{2}$ versus t_{spr} , the liquid contact front along with spreading to the time, at various T_w and $We = 113$. The curve of $r = \frac{D_t}{2}$ has an intersection with r_{pj} when peripheral jets occur, and the corresponding time is t_{pj} . Surprisingly, t_{pj} almost coincides with the end of t_{spr} , which is t_{ct} for most T_w , meaning that peripheral jets happen almost simultaneously with the beginning of film levitation. It implies that the vaporization of hemiwicking liquid could be the dominant reason for film levitation, and its dependence on T_w could be largely responsible for the impaired film levitation at a high T_w . Figure 8(b) shows the dependence of r_{pj} on T_w for various We . r_{pj} is substantially reduced at a high T_w , namely, peripheral jets emerging at a lower extent of spreading at a high T_w , while increasing We can enhance r_{pj} .

It is shown that a high T_w could lead to simultaneous occurrence of hemiwicking and vaporization, resulting in a smaller quantity of hemiwicking liquid to be vaporized. Moreover, at a high T_w , peripheral jets not only emerge earlier, but become so drastic that prevent further contact of droplet with the surface. The smaller contact area at the time of separation between the droplet and NTS can also lead to a smaller quantity of vapor in total. Moreover, after peripheral jets the remaining vapor in the nanotubes within the contact area is presumed to act as air pockets which are able to resist further liquid hemiwicking for a while, as evidenced by the fact that film levitation is barely discernible till the completion of peripheral jets and central jet at a high T_w . In contrast, at a low T_w , the vaporization rate is smaller, so peripheral jets appear at a relatively high extent of spread and are less drastic. The region of hemiwicking is thus relatively large, and the vapor stream produced enclosed by the droplet and the surface could have a large action area which is favored to push the droplet away from the surface as a film.

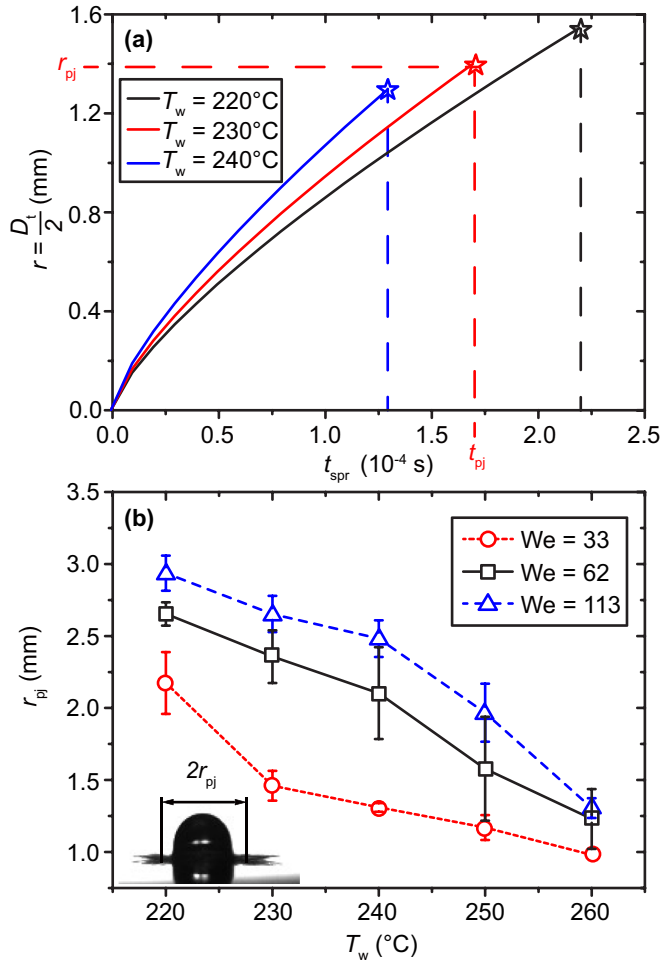


FIG. 8. (a) Contact radius $r = \frac{D_t}{2}$ as a function of the spread time t_{spr} with T_w at 220, 230, and 240°C . (b) Droplet contact radius at the commence of peripheral jets, r_{pj} , as a function of T_w with We at 33, 62, and 113. The inset image shows the contact radius r_{pj} of a droplet at the beginning of peripheral jets.

D. Mechanisms of central jet

Central jet emerges at high T_w . A high T_w leads to shorter vaporization time t_{ev} , hence the vapor stream coming out of the nanotubes in the central region right below the impact could bear a high upward velocity. Such a high speed vapor stream could pierce into the droplet bulk and drive a liquid jet to form. The maximum top height, h_{tmax} , and the bottom diameter, D_{cj} , of the central jet as a function of T_w for various We are, respectively, plotted in Figs. 9(a) and 9(b). h_{tmax} greatly increases at first, and then decreases by raising T_w . D_{cj} exhibits a similar trend that it increases gently first and then decreases rapidly with T_w . With an increase in T_w , vaporization of hemiwicking liquid is accelerated, so the vapor stream has a higher velocity and could exert a larger upward pressure at the droplet bottom. A higher T_w would also lead to a larger number of nanotubes in which the vaporization is strong enough to contribute to the formation of a central jet, manifested by the slight increase in D_{cj} for relatively low T_w . However, keep increasing T_w could enable vaporization to occur simultaneously with hemiwicking, during which the va-

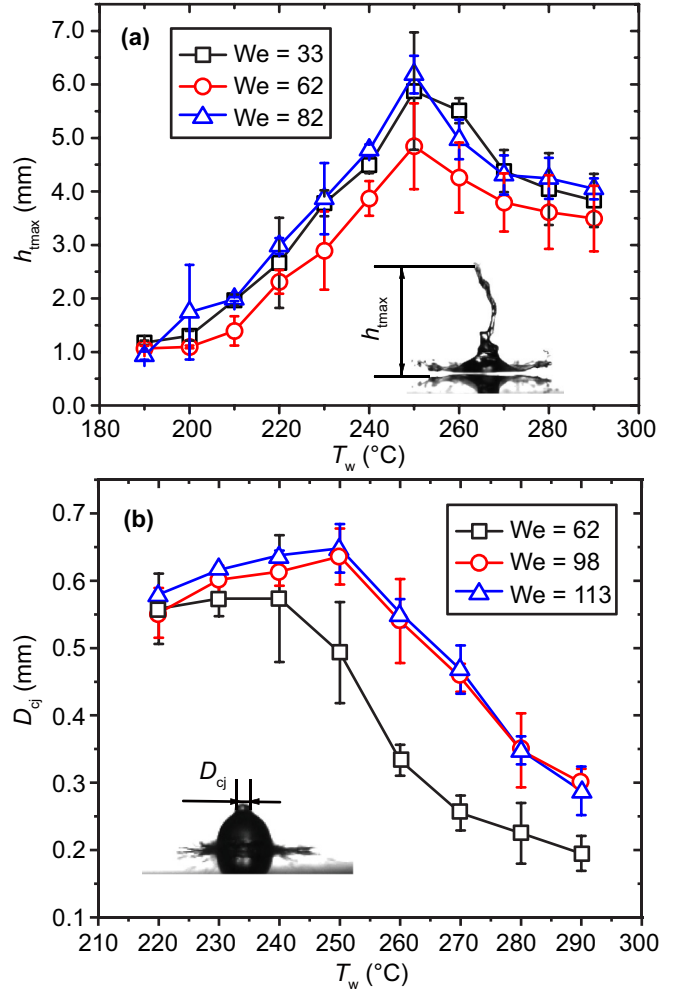


FIG. 9. (a) Maximum height of the central jet h_{tmax} as a function of T_w with We at 33, 62, and 82. The inset image indicates h_{tmax} of a droplet. (b) The diameter of the central jet D_{cj} as a function of T_w with We at 62, 98, and 113. The inset image indicates D_{cj} of a droplet.

por produced could resist upcoming hemiwicking and reduce the total hemiwicking liquid to be vaporized. Therefore, the action area of the vapor stream at the droplet bottom could become smaller, and the driving force led by vapor flow could be attenuated. These mechanisms collectively determine the ascending and then descending intensity of the central jet.

1. Force analysis on vapor stream driving central jet

Herein we conduct a force analysis on the vapor stream produced in the nanotubes within the projected area of the central jet to interpret the central jet phenomenon and its dependence of T_w . The vapor stream produced from massive nanotubes is acted upon by different forces at the moment of escape [see Fig. 10(a)] and when it pierces into the droplet bulk to form a central jet [Fig. 10(b)]. When the vapor in a nanotube is about to escape, it is acted upon by the driving force due to vapor volume expansion and capillary resistance due to the three-phase line forming at the interior wall of the nanotube. Moreover, since the droplet does not fully spread at the commence of central jet [see Figs. 2(c) and 2(d)], the vapor

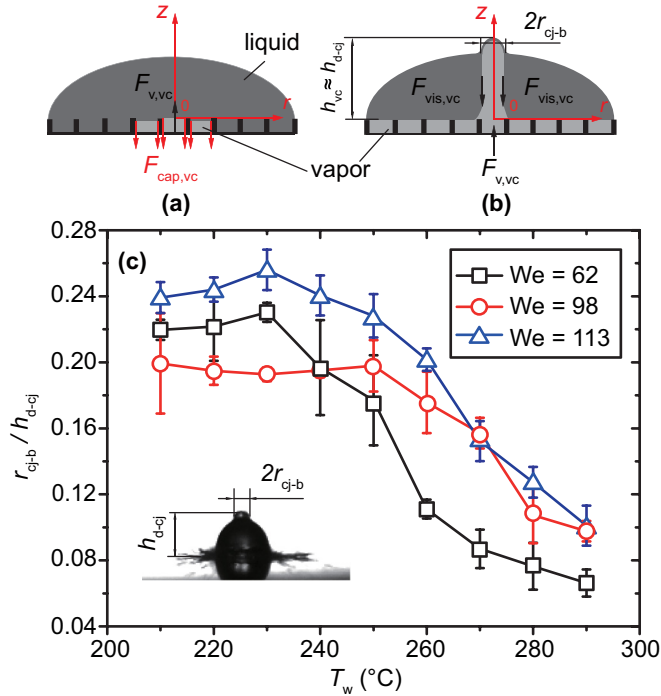


FIG. 10. Schematic diagram of the forces acting on the vapor stream (a) at the beginning of escape from nanotubes, and (b) when it pierces into the droplet to initiate a central jet for the central jet levitation (CJL) or central jet (CJ) regime. (c) The ratio of the central jet radius to the droplet central height at the commencement of central jet, $\frac{r_{cj-b}}{h_{d-cj}}$, versus the surface temperature T_w with We at 62, 98, and 113.

stream is also against by the droplet impact inertia. Lastly, once the vapor stream flows into the droplet bulk, whether a central jet would be formed is determined by that if the vapor stream is able to go through the instantaneous droplet height [see Fig. 10(b)]. Herein we analyze the competitions between the vapor driving force and the various resistances to probe the mechanism of central jet.

We made a number of assumptions that simplify the problem but could result in a deviation from the actual outcome. The first assumption is that the nanotube within the projected area of the central jet is fully filled with liquid through hemiwicking. The second one is that the vaporization is completed before its escape. Both the assumptions would lead to an over-estimation of the actual vapor pressure. These two assumptions allow us to obtain the vapor pressure P_v at the moment of escape from the nanotubes. The ethanol liquid is assumed to reach the saturation state corresponding to the atmospheric pressure during its hemiwicking before the vaporization is initiated, so the liquid density $\rho_l = 736.83 \text{ kg/m}^3$. According to mass conservation, the liquid mass filling a nanotube equals to the mass of vapor confined in the same nanotube before its escape, so the vapor density ρ_v is the same with ρ_l . By approximating the vapor temperature T_v to the surface temperature T_w , we can obtain P_v and viscosity μ_v of the vapor at the commence of escape by checking the NIST database, which shows that the vapor is at a superheated state.

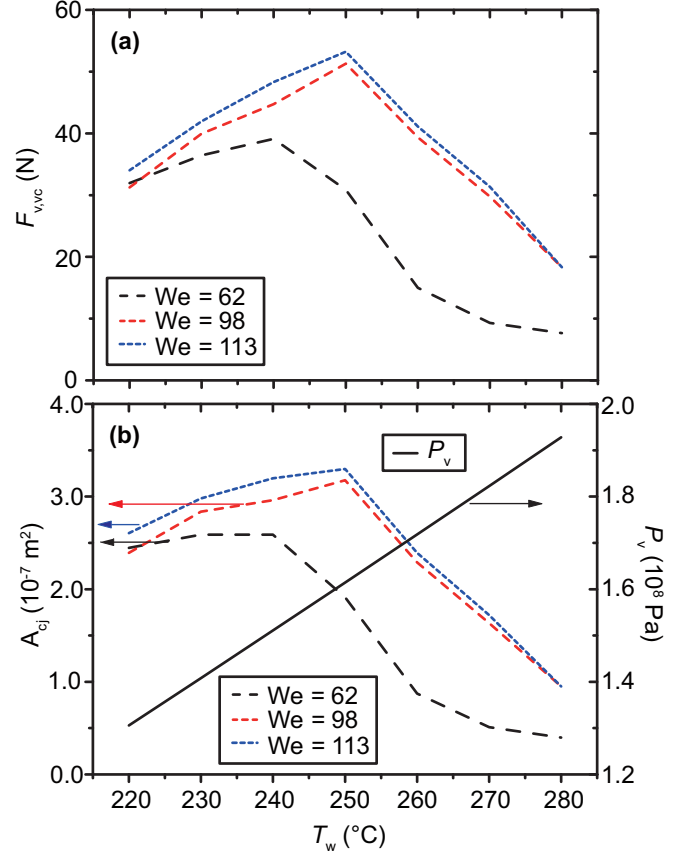


FIG. 11. (a) The driving force of the vapor stream $F_{v,vc}$ as a function of the surface temperature T_w with We at 62, 98, and 113, and (b) the cross-sectional area of the vapor stream A_{cj} and the vapor pressure P_v at the vapor escape from a nanotube.

By acquiring P_v , we can obtain the driving force of vapor in a single nanotube as $F_{v,n} = P_v \pi r_{in}^2$. Herein the vapor stream is seen converged by massive vapor columns produced in nanotubes in the projected area of the central jet. Since there are around $\frac{r_{cj-b}^2}{r_{out}^2}$ nanotubes in the projected area of the central jet, the total driving force $F_{v,vc} = A_{cj} P_v \approx \frac{r_{cj-b}^2}{r_{out}^2} \pi r_{in}^2 P_v$, where $A_{cj} \approx \frac{r_{cj-b}^2}{r_{out}^2} \pi r_{in}^2$ is the cross-sectional area of the vapor stream, and $r_{cj-b} \approx \frac{D_{cj}}{2}$ is the radius of the vapor stream which is regarded approximately to the bottom radius of the central jet. Figure 11(a) shows $F_{v,vc}$ as a function of T_w at three We . $F_{v,vc}$ increases first and then decreases, which is resulting from the collective effects of the dependencies of A_{cj} and P_v on T_w . As demonstrated in Fig. 11(b), A_{cj} increases at first and then decreases upon increasing T_w , while P_v increases with T_w , indicating that A_{cj} plays the main role in the variation of $F_{v,vc}$ with T_w . At a relatively low T_w , A_{cj} and P_v together enable the increase of the vapor driving force, while at a high T_w , for the same increment of T_w , the reciprocal of the declining multiplier of A_{cj} is greater than the increasing multiplier of P_v , so the vapor driving force begins to descend with T_w . It is speculated that $F_{v,vc}$ would be too small to initiate a central jet eventually if T_w were keep rising. In addition, by increasing We , the turning point of $F_{v,vc}$ is postponed and elevated. As

shown in Fig. 9(b), the diameter of the central jet D_{cj} is larger at a higher We , implying a larger cross-sectional area of the vapor stream, so the Leidenfrost point would be postponed at a higher We .

First, we compare the order of magnitudes of the driving force of vapor and the capillary force at the instant escape from nanotubes. Figure 10(a) schematically shows the two forces acting on the vapor stream at the beginning of escape from nanotubes. At the onset of escape, the liquid-vapor interface formed by the vapor and liquid is in contact with the upper inner edge of the nanotube, namely the capillary force acting upon the vapor stream is generated. Therefore, the vapor stream is acted upon by the driving force $F_{v,vc}$ and the capillary force $F_{cap,vc}$. The capillary force for a single nanotube is $F_{cap,n} = 2\pi r_{in}\sigma$, and the total capillary force for the vapor stream is $F_{cap,vc} \approx \frac{r_{cj-b}^2}{r_{out}^2} 2\pi r_{in}\sigma$. $\frac{F_{v,vc}}{F_{cap,vc}} = \frac{P_v r_{in}}{2\sigma} \sim 10^2$, so the effect of the capillary force be neglected.

Second, we compare the order of magnitudes of vapor driving force and droplet inertia on the vapor stream. When the droplet impacts onto the surface, the dynamic pressure P_d and the water hammer pressure P_{wh} are induced due to the inertia of the droplet. $P_d = 0.5\rho_l v_l^2$ and $P_{wh} = \rho_l v_s v_0$, where v_s is the speed of sound in ethanol [51]. At $We = 62$, $\frac{P_{wh}}{P_d} = \frac{2v_s v_0}{5v_l^2} \sim 10^2$, so P_d can be neglected. Therefore, the resistance due to the inertia of the droplet is $F_{ine,vc} = P_{wh}\pi r_{cj-b}^2$. It is worth to notice that $F_{ine,vc}$ obtained from this equation is the maximum since it is calculated by using the droplet impact velocity v_0 . After the impact, the downward flow velocity of the upper droplet decays with time substantially, so $F_{ine,vc}$ decays with time. By taking the case $T_w = 220^\circ\text{C}$ and $We = 62$ as an example, at the moment of vapor escape from nanotubes, $\frac{F_{v,vc}}{F_{ine,vc}} = \frac{r_{in}^2 P_v}{r_{out}^2 \rho_l v_l v_0} \sim 10^2$, so the effect of the droplet inertia can be neglected as well.

Third, as illustrated in Fig. 10(b), as the vapor stream pierces into the droplet bulk, it is driven by $F_{v,vc}$ while mainly against by the viscous force $F_{vis,vc}$. At the moment when the vapor stream reaches the droplet apex to initiate a central jet, the corresponding Reynolds number of the vapor stream can be expressed as $Re_v = \frac{2\rho_v v_v r_{cj-b}}{\mu_v}$, where ρ_v , μ_v , and v_v are corresponding to the vapor state at the beginning of central jet. v_v is calculated based on $P_v = \frac{1}{2}\rho_v v_v^2$ in which P_v also corresponds to the vapor pressure at the beginning of central jet. Re_v is at the order of 10^7 with T_w at 220°C and We at 62 as an example, so the vapor flow can be approximated as a turbulent flow. The velocity of a turbulent flow is resemblance to a plug flow such that the velocity profile is uniform while exhibits a steep decline near the wall [52–54]. Due to the fact that we are unable to obtain such a velocity profile, it is difficult to obtain the viscous stress at the liquid-vapor interface. But we could refer to the liquid-vapor friction factor f_i of an annular flow to estimate the viscous force at the liquid-vapor interface of the central jet.

The Weber number of the vapor stream at the beginning of a central jet is $We_v \approx \frac{\rho_v v_v^2 D_{cj}}{\sigma} \approx 10^4$, where ρ_v , σ , and v_v corresponds to the beginning of a central jet. For the liquid phase, its velocity is approximated as the initial moving velocity of the central jet such that $We_l \approx \frac{\rho_l v_l^2 D_{cj}}{\sigma} \approx 10^2$, where v_l is the

averaged velocity of the central jet over the first 0.14 ms from its beginning of formation. It was observed in the experiment that most central jets were fractured or pierced by the vapor stream, implying that v_v is much higher than v_l . If we apply the identification of the two-phase flow regime, the two Weber numbers suggest an annular flow [55], and the corresponding interfacial friction factor at the vapor-liquid interface can be expressed as $f_i = 0.005[1 + 300\delta/D_{cj}]$, where δ is the film thickness of the liquid phase [56]. To simplify the analysis, we assume that the film thickness of the liquid is extremely thin such that it is nearly 0, so we obtain the minimum f_i . Combining $f_i = 2\tau_i/(\rho_v v_v^2)$ and $F_{vis,vc} \approx 2\pi r_{cj-b} h_{vc} \tau_i$, we obtain the expression of the viscous force $F_{vis,vc} \approx \pi r_{cj-b} h_{vc} f_i \rho_v v_v^2$, where τ_i is the shear stress at the vapor-liquid interface and h_{vc} is the distance traveled by the vapor stream in the droplet.

The ratio of $F_{v,vc}$ to $F_{vis,vc}$ is $\frac{F_{v,vc}}{F_{vis,vc}} = (\frac{1}{2} \frac{r_{in}^2}{r_{out}^2 f_i}) (\frac{r_{cj-b}}{h_{d-cj}})$, and a central jet would be formed if this ratio is higher than unity when the vapor moving distance h_{vc} reaches the instantaneous droplet central height h_{d-cj} . This relation gives $(\frac{r_{cj-b}}{h_{d-cj}}) > 0.02$, implying a criterion for the emergence of a central jet phenomenon in respect to the relation between the central jet radius and the instantaneous droplet central height when the vapor flow reaches the droplet apex. The ratio $(\frac{r_{cj-b}}{h_{d-cj}})$ measured from the experiment for various T_w and We are plotted in Fig. 10(c). It can be seen that all the values are greater than the predicted threshold of $(\frac{r_{cj-b}}{h_{d-cj}})$, and the minimum measured value is 0.06 which is at the same order of magnitude, confirming the rationality of the theoretical analysis. Moreover, the ratio $\frac{F_{v,vc}}{F_{vis,vc}} = (\frac{1}{2} \frac{r_{in}^2}{r_{out}^2 f_i}) (\frac{r_{cj-b}}{h_{d-cj}})$ reflects the intensity of the central jet, and its variation with T_w should be similar to that of $(\frac{r_{cj-b}}{h_{d-cj}})$ such that it increases first and then decreases with an increase in T_w . This trend resembles to that of $F_{v,vc}$, again confirming the major role of the cross-sectional area of a vapor stream in determining the central jet behavior.

2. Energy analysis on central jet

Here we conduct an energy analysis on the impact process to further probe the interplay of vapor and droplet dynamics and how it is affected by T_w . The vapor produced upon droplet impact onto NTS has a high kinetic energy that gives rise to the droplet levitation and liquid central jet. Such kinetic energy can be divided to two parts. One is the kinetic energy $E_{k,v1}$ of vapor produced by hemiwicking liquid in the central contact area. It mainly enables the motion of the central jet, and is comprised of the kinetic energy $E_{k,cj}$, the potential energy change ΔE_p , the surface energy change ΔE_s and the viscous dissipation E_{vis} of the central jet, and the kinetic energy $E_{k,vr}$ of the escaping vapor. The other is the kinetic energy $E_{k,v2}$ of vaporization outside the central region, comprised of vaporization of both the droplet bottom layer above nanotubes and hemiwicking liquid. It contributes to the levitation kinetics, potential energy change, surface energy change and viscous dissipation of the bulk droplet, and the kinetic energy of the escaping vapor. Herein the estimation of $E_{k,v2}$ could be very complex, and to simply the analysis we solely examine the energy distribution of $E_{k,v1}$ and its influence on the overall droplet dynamics.

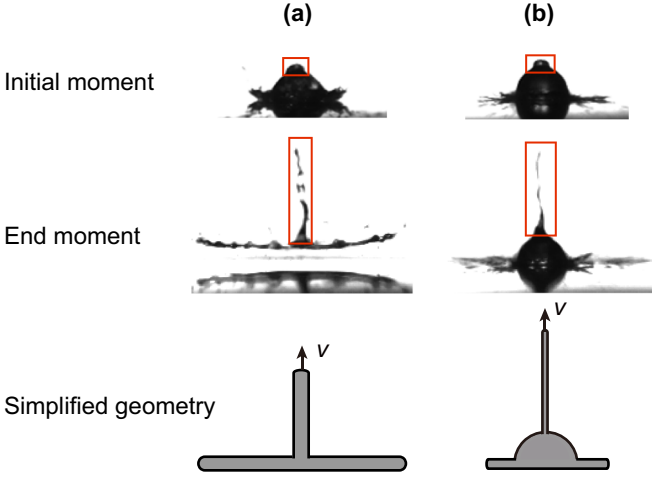


FIG. 12. The initial and end moments, and the simplified geometry of the central jet in (a) central jet levitation (CJL) and (b) central jet (CJ) regimes.

To simplify the calculation of the droplet surface area and volume, as shown in Fig. 12(a), for CJL regime, the droplet bulk is treated as a pancake and the central jet as a cylinder. For CJ regime, the bulk is seen as a combination of a pancake and a part of a sphere and the central jet as a cylinder, as shown in Fig. 12(b). The time for the central jet about to form is indicated as the initial moment t_1 , and the moment at the fracture of the central jet is indicated as the end moment t_2 , at which a portion of vapor escapes through piercing the central jet.

$E_{k,v1}$ is regarded as the vapor kinetic energy originated from the vaporization of hemi-wicking liquid in the projected area of the central jet, and $E_{k,v1} = \frac{1}{2}m_v v_v^2$, where m_v is the vapor mass produced by hemi-wicking liquid in the projected area of the central jet. $m_v \approx A_{cj} \rho_{l,a} h_n$. The energy difference of the central jet at t_1 and t_2 is indicated as ΔE , and $\Delta E = E_2 - E_1 = E_{k,cj} + E_{vis} + \Delta E_p + \Delta E_s$. The kinetic energy is $E_{k,cj} = \frac{1}{2}m_{cj} \bar{v}_{cj}^2$, in which m_{cj} is the central jet mass, $\bar{v}_{cj} = \frac{v_{cj-t}}{2}$ the arithmetic average velocity of the central jet, and v_{cj-t} is the velocity at the central jet top. The viscous dissipation is $E_{vis} = \int_{t_1}^{t_2} \phi dV dt \approx \phi V_{cj}(t_2 - t_1)$, where $\phi \approx \mu_l (\frac{\Delta v_{cj}^2}{h_{cj}})$ [57], in which Δv_{cj} is the velocity difference of the central jet at t_1 and t_2 , h_{cj} the central jet length, $V_{cj} = \pi \bar{r}_{cj}^2 h_{cj}$ the volume of the central jet, $\bar{r}_{cj} = (r_{cj-b} + r_{cj-t})/2$ the arithmetic average radius of the central jet, and r_{cj-t} is the radius of the central jet top. The potential energy change is $\Delta E_p = m_{cj} g \Delta h$, in which Δh is the distance between the mass centers of the central jet and droplet bulk, and g is the gravitational acceleration. The surface energy change of the central jet is $\Delta E_s = \Delta A \sigma$, where ΔA is the change of surface area of the central jet from t_1 to t_2 . The kinetic energy taken away by the escaping vapor, $E_{k,vr}$, is approximately equivalent to the difference between $E_{k,v1}$ and ΔE , namely, $E_{k,vr} \approx E_{k,v1} - \Delta E$.

Here we examine the cases with $We = 62$ and 82 , and $220^\circ\text{C} \leq T_w \leq 280^\circ\text{C}$ as examples, and the various types of energy as functions of T_w are plotted in Fig. 13. $E_{k,v1}$ increases and then decreases with T_w for both We , and the turning point is in the vicinity of the transition from the regime of CJL to

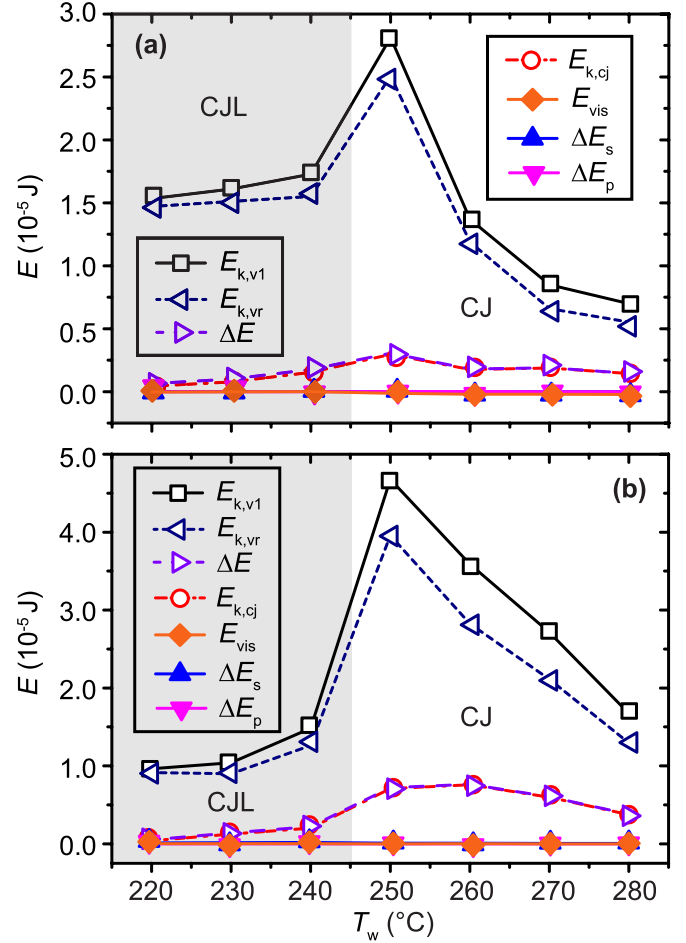


FIG. 13. The kinetic energy $E_{k,v1}$ of the vapor produced by hemi-wicking liquid in the central projected area of the central jet, the kinetic energy $E_{k,vr}$ of the escape vapor, the energy difference ΔE of the central jet, the kinetic energy $E_{k,cj}$ of the central jet, the viscous dissipation E_{vis} of the central jet, the surface energy change ΔE_s of the central jet, and the potential energy change ΔE_p as a function of the surface temperature T_w at (a) $We = 62$ and (b) $We = 82$.

CJ featuring earlier emergence of peripheral jets. It implies that the vaporization for film levitation and central jet begin to be weakened at an analogous T_w , and that vaporization of hemiwicking should be the dominant mechanism for film levitation. The trend of $E_{k,v1}$ resembles that of vapor driving force $F_{v,vc}$, indicating again the collective effects of decreasing quantity of vapor while increasing pressure of vapor upon increasing T_w .

At a relatively low T_w , $E_{k,v1}$ is largely transferred to $E_{k,vr}$, so the escaping vapor takes away the majority of the vapor kinetic energy. In the regime of CJL corresponding to a low range of T_w , the droplet is levitated entirely, so a portion of the vapor produced from the central nanotubes can escape through the path between the droplet bottom and NTS, resulting in the large $E_{k,vr}$. Upon increasing T_w , both $E_{k,vr}$ and $E_{k,v1}$ are reduced significantly, meanwhile $E_{k,cj}$ and its fraction in $E_{k,v1}$ are both increased. In the regime of CJ corresponding to a high range of T_w , film levitation does not occur, thus the vapor produced from the central nanotubes can solely escape through piercing the central jet. As a result, $E_{k,vr}$ becomes smaller,

but still dominates the dissipation of $E_{k,v1}$. $E_{k,cj}$, the kinetic energy of the central jet, increases to become an important dissipation of $E_{k,v1}$. The latter descending trend of $E_{k,cj}$ at high T_w is attributed to the decreasing total vapor kinetic energy. In addition, E_{vis} , ΔE_p and ΔE_s are several orders of magnitude smaller than $E_{k,vr}$ and $E_{k,cj}$, and they barely fluctuate with T_w , so the curves of $E_{k,cj}$ and ΔE are almost overlapped, as demonstrated in Fig. 13.

IV. CONCLUSIONS

We experimentally investigated the collective effects of surface temperature and surface nanotubes on the thermodynamics of an ethanol droplet. Five distinct regimes of impact droplet were observed, among which the regimes of film levitation, central jet levitation, and central jet were found induced by surface nanotubes. These regimes mainly featured in levitation of the droplet bulk and/or the liquid jet at the droplet center. Film levitation was mainly attributed to the vaporization of hemiwicking liquid in nanotubes of the contact area, and droplet bottom layer above the nanotube structure. Such vaporization was negatively dependent on the surface temperature, which accounted for the attenuated film levitation upon increasing the surface temperature. The central jet phenomenon was caused by the vaporization of hemiwick-

ing liquid in the central area upon impact. It was enhanced while then suppressed by increasing the surface temperature, resulting from the collective effects of the increased vapor pressure, and the cross-sectional area of the vapor stream which increased and then decreased with the surface temperature. The different parts of vaporization interacted and affected the energy distribution, which in turn modified the droplet dynamics. Due to the nanotube structures, the Leidenfrost point which occurred at 180°C on the plain titanium surface was increased to 230°C on the nanotube surface at a low We of 17, while it was increased by at least 125°C at high We . This study revealed the mechanisms and characteristics of an impact droplet on a nanotube surface at superheated conditions. The findings suggested a strategy to enhance the heat transfer by delaying the Leidenfrost point, and to manipulate droplet behaviors for droplet-based techniques.

ACKNOWLEDGMENTS

The authors are grateful for the financial support by the National Natural Science Foundation of China (Grant No. 51806163), and the Fundamental Research Funds for the Central Universities (Grants No. ND6J005 and No. xjh012019017).

-
- [1] M. R. O. Panão and A. L. N. Moreira, Flow characteristics of spray impingement in PFI injection systems, *Exp. Fluids* **39**, 364 (2005).
 - [2] M. Pasandideh-Fard, S. D. Aziz, S. Chandra, and J. Mostaghimi, Cooling effectiveness of a water drop impinging on a hot surface, *Int. J. Heat Fluid Flow* **22**, 201 (2001).
 - [3] J. H. Kim, Spray cooling heat transfer: The state of the art, *Int. J. Heat Fluid Flow* **28**, 753 (2007).
 - [4] G. T. Liang and I. Mudawar, Review of drop impact on heated walls, *Int. J. Heat Mass Transf.* **106**, 103 (2017).
 - [5] N. Lipson and S. Chandra, Cooling of porous metal surfaces by droplet impact, *Int. J. Heat Mass Transf.* **152**, 119494 (2020).
 - [6] J. Rodrigues and S. Desai, The nanoscale Leidenfrost effect, *Nanoscale* **11**, 12139 (2019).
 - [7] J. G. Leidenfrost, On the fixation of water in diverse fire, *Int. J. Heat Mass Transf.* **9**, 1153 (1966).
 - [8] W. Bouwhuis, K. G. Winkels, I. R. Peters, P. Brunet, D. V. D. Meer, and J. H. Snoeijer, Oscillating and star-shaped drops levitated by an airflow, *Phys. Rev. E* **88**, 023017 (2013).
 - [9] S. M. Chen and V. Bertola, Jumps, somersaults, and symmetry breaking in Leidenfrost drops, *Phys. Rev. E* **94**, 021102(R) (2016).
 - [10] K. Piroird, C. Clanet, and D. Quéré, Magnetic control of Leidenfrost drops, *Phys. Rev. E* **85**, 056311 (2012).
 - [11] J. C. Burton, A. L. Sharpe, R. C. A. van der Veen, A. Franco, and S. R. Nagel, Geometry of the Vapor Layer under a Leidenfrost Drop, *Phys. Rev. Lett.* **109**, 074301 (2012).
 - [12] A. B. Wang, C. H. Lin, and C. C. Chen, The critical temperature of dry impact for tiny droplet impinging on a heated surface, *Phys. Fluids* **12**, 1622 (2000).
 - [13] L. S. Zhong and Z. G. Guo, Effect of surface topography and wettability on the Leidenfrost effect, *Nanoscale* **9**, 6219 (2017).
 - [14] L. Xu, L. Barcos, and S. R. Nagel, Splashing of liquids: Interplay of surface roughness with surrounding gas, *Phys. Rev. E* **76**, 066311 (2007).
 - [15] E. R. Negeed, S. Hidaka, M. Kohno, and Y. Takata, Effect of the surface roughness and oxidation layer on the dynamic behavior of micrometric single water droplets impacting onto heated surfaces, *Int. J. Therm. Sci.* **70**, 65 (2013).
 - [16] Y. S. Ko and S. H. Chung, An experiment on the breakup of impinging droplets on a hot surface, *Exp. Fluids* **21**, 118 (1996).
 - [17] J. D. Bernardin and I. J. Mudawar, The Leidenfrost point: Experimental study and assessment of existing models, *J. Heat Transfer* **121**, 894 (1999).
 - [18] M. Khavari, C. Sun, D. Lohse, and T. Tran, Fingering patterns during droplet impact on heated surfaces, *Soft Matter* **11**, 3298 (2015).
 - [19] H. J. J. Staat, T. Tran, B. Geerdink, G. Riboux, C. Sun, J. M. Gordillo, and D. Lohse, Phase diagram for droplet impact on superheated surfaces, *J. Fluid Mech.* **779**, R3 (2015).
 - [20] G. Liang, S. Shen, Y. Guo, and J. Zhang, Boiling from liquid drops impact on a heated wall, *Int. J. Heat Mass Transf.* **100**, 48 (2016).
 - [21] L. Xu, W. W. Zhang, and S. R. Nagel, Drop Splashing on a Dry Smooth Surface, *Phys. Rev. Lett.* **94**, 184505 (2005).
 - [22] C. S. Stevens, A. Latka, and S. R. Nagel, Comparison of splashing in high- and low-viscosity liquids, *Phys. Rev. E* **89**, 063006 (2014).
 - [23] A.-B. Wang, C.-H. Lin, and C.-C. Cheng, Pattern analysis of a single droplet impinging onto a heated plate, *Heat Transf. Asian Res.* **34**, 579 (2005).

- [24] S.-L. Chiu and T.-H. Lin, Experiment on the dynamics of a compound drop impinging on a hot surface, *Phys. Fluids* **17**, 122103 (2005).
- [25] A.-L. Bianco, F. Chevy, C. Clanet, G. Lagubeau, and D. Quéré, On the elasticity of an inertial liquid shock, *J. Fluid Mech.* **554**, 47 (2006).
- [26] P. Tsai, M. H. Hendrix, R. R. Dijkstra, L. Shui, and D. Lohse, Microscopic structure influencing macroscopic splash at high weber number, *Soft Matter* **7**, 11325 (2011).
- [27] T. Tran, H. Staat, A. Prosperetti, C. Sun, and D. Lohse, Drop Impact on Superheated Surfaces, *Phys. Rev. Lett.* **108**, 036101 (2012).
- [28] M. Shirota, M. A. J. van Limbeek, C. Sun, A. Prosperetti, and D. Lohse, Dynamic Leidenfrost Effect: Relevant Time and Length Scales, *Phys. Rev. Lett.* **116**, 064501 (2016).
- [29] A. F. A. Karl, Experimental investigation of interaction processes between droplets and hot walls, *Phys. Fluids* **12**, 785 (2000).
- [30] R. Munoz, D. Beving, and Y. Yan, Hydrophilic zeolite coatings for improved heat transfer, *Ind. Eng. Chem. Res.* **44**, 4310 (2005).
- [31] C. T. Avedisian and J. Koplik, Leidenfrost boiling of methanol droplets on hot porous/ceramic surfaces, *Int. J. Heat Mass Transf.* **30**, 379 (1987).
- [32] C. Kruse, T. Anderson, C. Wilson, C. Zuhlke, D. Alexander, G. Gogos, and S. Ndao, Extraordinary shifts of the Leidenfrost temperature from multiscale micro/nanostructured surfaces, *Langmuir* **29**, 9798 (2013).
- [33] R. L. Agapov, J. B. Boreyko, D. P. Briggs, B. R. Srijanto, S. T. Retterer, C. P. Collier, and N. V. Lavrik, Length scale of Leidenfrost ratchet switches droplet directionality, *Nanoscale* **6**, 9293 (2014).
- [34] C. M. Weickgenannt, Y. Y. Zhang, S. Sinha-Ray, I. V. Roisman, T. Gambaryan-Roisman, C. Tropea, and A. L. Yarin, Inverse-Leidenfrost phenomenon on nanofiber mats on hot surfaces, *Phys. Rev. E* **84**, 036310 (2011).
- [35] S. H. Kim, H. S. Ahn, J. Kim, M. Kaviany, and M. H. Kim, Dynamics of water droplet on a heated nanotubes surface, *Appl. Phys. Lett.* **102**, 233901 (2013).
- [36] V. Talari, P. Behar, Y. Lu, E. Haryadi, and D. Liu, Leidenfrost drops on micro/nanostructured surfaces, *Front. Energy* **12**, 22 (2018).
- [37] J. Bico, U. Thiele, and D. Quéré, Wetting of textured surfaces, *Colloids Surf. A* **206**, 41 (2002).
- [38] H. Kim, B. Truong, J. Buongiorno, and L. W. Hu, On the effect of surface roughness height, wettability, and nanoporosity on Leidenfrost phenomena, *Appl. Phys. Lett.* **98**, 083121 (2013).
- [39] H. M. Kwon, J. C. Bird, and K. K. Varanasi, Increasing Leidenfrost point using micro-nano hierarchical surface structures, *Appl. Phys. Lett.* **103**, 201601 (2013).
- [40] N. Farokhnia, S. M. Sajadi, P. Irajizad, and H. Ghasemi, Decoupled hierarchical structures for suppression of Leidenfrost phenomenon, *Langmuir* **33**, 2541 (2017).
- [41] W. Tong, L. Qiu, J. Jin, L. D. Sun, and F. Duan, Unique lift-off of droplet impact on high-temperature nanotube surfaces, *Appl. Phys. Lett.* **111**, 091605 (2017).
- [42] H. Hu, C. Xu, Y. Zhao, R. Shaeffer, K. J. Ziegler, and J. N. Chung, Modification and enhancement of cryogenic quenching heat transfer by a nanoporous surface, *Int. J. Heat Mass Transf.* **80**, 636 (2015).
- [43] H. Nair, H. J. J. Staat, T. Tran, A. van Houselt, A. Prosperetti, D. Lohse, and C. Sun, The Leidenfrost temperature increase for impacting droplets on carbon-nanofiber surfaces, *Soft Matter* **10**, 2102 (2014).
- [44] L. Sun, X. Wang, M. Li, S. Zhang, and Q. Wang, Anodic titania nanotubes grown on titanium tubular electrodes, *Langmuir* **30**, 2835 (2014).
- [45] See Supplemental Material at <http://link.aps.org/supplemental/10.1103/PhysRevE.102.043108> for a video of five droplet regimes (contact boiling, film levitation, central jet levitation, central jet, and Leidenfrost phenomenon) with the initial diameter of 1.62 mm at different surface temperatures and Weber numbers.
- [46] A. I. Aria and M. Gharib, Physicochemical characteristics and droplet impact dynamics of superhydrophobic carbon nanotube arrays, *Langmuir* **30**, 6780 (2014).
- [47] S. H. Kim, G. Lee, H. Kim, and M. H. Kim, Leidenfrost point and droplet dynamics on heated micropillar array surface, *Int. J. Heat Mass Transf.* **139**, 1 (2019).
- [48] M. Seki, H. Kawamura, and K. Sanokawa, Transient temperature profile of a hot wall due to an impinging liquid droplet, *J. Heat Transfer* **100**, 167 (1978).
- [49] J. Kim, M. W. Moon, and H. Y. Kim, Dynamics of hemiwicking, *J. Fluid Mech.* **800**, 57 (2016).
- [50] F. McGinnis and J. Holman, Individual droplet heat-transfer rates for splattering on hot surfaces, *Int. J. Heat Mass Transf.* **12**, 95 (1969).
- [51] T. Deng, K. K. Varanasi, M. Hsu, N. Bhate, C. Keimel, J. Stein, and M. Blohm, Nonwetting of impinging droplets on textured surfaces, *Appl. Phys. Lett.* **94**, 133109 (2009).
- [52] J. Eggers, Universal Pinching of 3D Axisymmetric Free-Surface Flow, *Phys. Rev. Lett.* **71**, 3458 (1993).
- [53] P. Doshi, I. Cohen, W. W. Zhang, M. Siegel, P. Howell, O. A. Basaran, and S. R. Nagel, Persistence of memory in drop breakup: The breakdown of universality, *Science* **302**, 1185 (2003).
- [54] R. Suryo, P. Doshi, and O. A. Basaran, Non-self-similar, linear dynamics during pinch-off of a hollow annular jet, *Phys. Fluids* **16**, 4177 (2004).
- [55] L. Chen, Y. S. Tian, and T. G. Karayiannis, The effect of tube diameter on vertical two-phase flow regimes in small tubes, *Int. J. Heat Mass Transf.* **49**, 4220 (2006).
- [56] G. B. Wallis, *One Dimensional Two-Phase Flow* (McGraw-Hill, New York, 1969).
- [57] S. Chandra and C. T. Avedisian, On the collision of a droplet with a solid surface, *Proc. R. Soc. London A* **432**, 13 (1991).